Research Article

Maisarah Mansor, Nadiah Husseini Zainol Abidin*, Norita Mohd Yusoff, Kuen Yao Lau, Josephine Liew Ying Chyi, Vijay Janyani, Amit Kumar Garg, Mohammed Thamer Alresheedi, and Mohd Adzir Mahdi

Tungsten trioxide nanocomposite for conventional soliton and noise-like pulse generation in anomalous dispersion laser cavity

https://doi.org/10.1515/ntrev-2022-0535
received August 18, 2022; accepted March 14, 2023

Abstract: This work demonstrates the employment of tungsten trioxide/polydimethylsiloxane nanocomposite saturable absorber (WO_3/PDMS-SA) in realizing mode-locked conventional soliton (CS) and noise-like pulse (NLP) laser generation in net anomalous dispersion. The switching formation from CS regime of 970.0 fs pulse duration to NLP regime of 182.0 fs coherent spike with 65.3 ps pedestal was achieved by varying its pump power. The pulse laser exhibited good stability of 50.76 and 49.82 dB signal-to-noise ratio at 9.09 MHz fundamental repetition rate and trivial variation during stability test for CS and NLP regime, respectively. This work expresses the feasibility of WO_3/PDMS-SA in attaining various types of mode-locked pulse phenomena using a fixed cavity configuration conceivably beneficial for compact dual-purpose laser systems.

Keywords: tungsten trioxide, mode-locked fiber laser, tapered optical fiber

*** Corresponding author: Nadiah Husseini Zainol Abidin,** Wireless and Photonics Networks Research Centre, Faculty of Engineering, Universiti Putra Malaysia, 43400 UPM Serdang, Selangor, Malaysia, e-mail: hza_nadiah@upm.edu.my
Maisarah Mansor, Norita Mohd Yusoff, Mohd Adzir Mahdi: Wireless and Photonics Networks Research Centre, Faculty of Engineering, Universiti Putra Malaysia, 43400 UPM Serdang, Selangor, Malaysia
Kuen Yao Lau: State Key Laboratory of Modern Optical Instrumentation, College of Optical Science and Engineering, Zhejiang University, Hangzhou 310027, China
Josephine Liew Ying Chyi: Department of Physics, Faculty of Science, Universiti Putra Malaysia, 43400 UPM Serdang, Selangor, Malaysia
Vijay Janyani: Department of Electronics and Communication Engineering, Malaviya National Institute of Technology, Jaipur, India
Amit Kumar Garg: Department of Electronics and Communication Engineering, Indian Institute of Information Technology, Kota (MNIT Campus), Jaipur, India
Mohammed Thamer Alresheedi: Department of Electrical Engineering, College of Engineering, King Saud University, P.O. Box 800, Riyadh 11421, Kingdom of Saudi Arabia

1 Introduction

The advancement of ultrafast science has provided mankind with techniques to observe, analyze, and manipulate dynamic responses to further progress other scientific fields and technology [1]. Pulse duration in order of tens of attoseconds based on high harmonic generation in the extreme ultraviolet region [2] has led to the development of highly-sensitive spectroscopy used to measure the phase difference between isotopes [3]. Another technology within the ultrafast science field receiving rising interest is the ultrafast fiber laser. Ultrafast fiber laser has been widely used in numerous cutting-edge applications due to their extremely narrow pulse duration, reproducible simple structure, and the potential for high intensity pulse energy. Applications in various fields include laser precision engineering that fabricates micron to nano-sized functional structures [4,5], medical treatments [6], biomaterials [7], and nonlinear optics [8–10]. In particular, the passively mode-locked ultrafast fiber laser (MLFL) based on a saturable absorber (SA) has also emerged as one of the most powerful strategies to develop ultrashort pulses (<1 ps) because of their benefits of high beam quality, low cost, efficient structure, alignment-free compact design, and excellent compatibility [11]. They also provide an ideal platform for exploring new areas of nonlinear dynamics in an open, dissipative environment, where various physical effects can experience significant interactions [12]. These effects include dispersion effects, nonlinear Kerr effects, linear and nonlinear birefringence, dissipation effects, and gain bandwidth limitations. These physical effects lead to the formation and generation of various optical pulses by

changing the structure and adjusting the parameters of the cavity.

Dissipative soliton (DS) originates from the composite balancing of several effects which includes nonlinearity, dispersion, gain, and loss [13]. DS is typically formed in net normal dispersion, but it has been proven to exist whether the average dispersion of the cavity is anomalous, normal, or zero by fulfilling the composite balance condition [14,15]. DS features stable, largely chirped pulses with steep edges, and with energy up to hundreds of nJ. In contrast, the formation of conventional soliton (CS) with distinct Kelly sidebands in net anomalous dispersion cavity is dominated by the balancing effect between group velocity dispersion (GVD) and nonlinear effect of self-phase modulation [13]. Meanwhile, the imbalance between the aforesaid effects may favor a pulse splitting into multi-soliton states; which can be in the form of bound-state soliton, harmonic soliton molecules, soliton rain, and noise-like pulse (NLP) [16–18]. The dynamic behavior of mode-locked transient regimes can be investigated in real-time *via* the dispersive Fourier transform technique, which stretches the optical pulse in time domain while propagating in a dispersive medium [19,20]. This technique accurately maps the spectral information onto the time domain, such that the stretched temporal intensity has the same form as the pulse spectrum.

In general, NLP is marked by its high pulse energy, broad optical spectrum, and relatively weak temporal coherence [21]. For these reasons, NLP has been widely used in a number of applications such as in micromachining [22] as a supercontinuum source [23] and in photoluminescence spectroscopy [24]. Another unique feature of NLP is the ability to exist in all dispersion regimes. The simulation in ref. [25] suggested that the difference between NLP formation in normal and anomalous dispersion regime is the pulse compressibility, where a chirp-free pulse in the anomalous regime is incompressible compared to its counterpart with an up-chirp distribution trend. In the near-zero net cavity GVD, the higher nonlinearity enhances self-phase modulation during peak power growth for potentially wider spectral broadening [26]. However, in this regime, a modulator of higher contrast is necessary to stabilize the pulse generation [27].

The challenge of further narrowing the pulse duration and pulse energy scalability which are key obstacles of CS in anomalous dispersion regime can also easily be addressed by NLP. Investigations on the pulse dynamics from CS to NLP have been experimentally established in different cavity designs such as figure-of-eight with amplifying loop mirror [28], optical loop mirror [29,30], as well as nonlinear polarization rotation (NPR) [31–33]. In the accompaniment of a nonlinear material-based SA, the manipulation of cavity settings; namely state of intracavity polarization, dispersion management, and pump power [34] may also tailor the saturable absorption effect, which leads to an alternate formation of fundamental pulse to sub-pulses of varying phases and random amplitudes observed with NLP. The formation of NLP from another pulse phenomena has been linked to the growth of peak power initiating two-photon absorption (TPA) and reverse saturable absorption (RSA) consequently bringing forth peak power clamping into effect [35]. The complement effect of soliton collapse and positive cavity feedback (from self-phase modulation) at high gain conditions typically observed at near-zero dispersion can also switch the CS regime to NLP regime [32].

Material-based SAs is one of the straightforward routes which can yield NLP by pump power variation. Carbon nanotubes (CNT)-SA employed in a 1.9 μm laser cavity with GVD of 1.63 ps^2, generated 5.1 nm bandwidth of NLP at 650 mW pump power [36]. In the same wavelength band, external amplification of NLP has been proposed to up-scale the pulse energy and avoid threshold damage to the graphene/polymer composite fiber ferrule-based SA, emitting 51.5 nJ pulse energy at 6 W pump power [37]. In another work, both DS and NLP have been demonstrated by employing a CNT/graphene composite SA, where the output was tuned by simply stretching a chirped fiber Bragg grating [38]. Up to 8.8 nJ pulse energy have been generated by integrating tellurene-SA and tungsten disulfide-SA in a laser cavity with net GVD of 0.096 [39] and –0.92 ps^2 [40], respectively. Other than that, numerous soliton phenomena including single and multi-soliton as well as NLP have been observed in an erbium-doped fiber (EDF) laser by the employment of topological insulator-SA with net GVD of –3.09 ps^2 [17].

In recent years, tungsten trioxide (WO_3), a type of transition metal oxide (TMO) has been under the spotlight for its excellent nonlinear properties. TMOs in general are very stable at room temperature with high thermal stability [41]. The pioneer work on WO_3-SA was based on a thin-film SA sandwiched between two fiber ferrules with modulation depth (MD) of 20% and low saturation intensity (I_{sat}) of 0.04 MW/cm^2 [42]. However, the length of laser cavity was over 100 m that caused the reduction of spectral bandwidth as a result of longer pulse duration. The most common issue faced by sandwich type SAs is the low damage threshold caused by perpendicular illumination over a small area of few μm^2 where the laser directly interacts with the material and the small interaction area leads to poor heat dissipation. In contrast, the use of tapered optical fiber as a substrate for nonlinear optical material is able to circumvent these issues without adding

complexity to the fabrication process. The core/cladding of a standard single-mode fiber (SMF) is simply fused together and reduced significantly to 10–30 μm in diameter. In the fuse zone, propagating light is no longer confined to the core and can propagate outside the fiber as evanescent field *via* silica/air guiding to interact with the deposited nonlinear material. The lateral interaction of light with the material allows for increased nonlinear interaction length and effective heat dissipation. The small waist diameter of the tapered fiber structure also heightens the nonlinearity of the device without compromising the nonlinear material when operated at higher pump powers [43,44]. Ultimately, the use of tapered fiber produces SAs with high optical damage threshold that supports operation in high power regimes and the generation of high energy pulses [45]. Additionally, polymer such as polydimethylsiloxane (PDMS) is one of the reputed polymers in SA integration, featuring high porosity yet with hydrophobic characteristic. It has a low thermo-optic coefficient, is non-volatile, non-toxic, and has high transparency from the ultraviolet toward the near-infrared band. PDMS has a refractive index of 1.3997 at 1,554 nm wavelength which supports efficient back-coupling of the evanescent wave compared to air.

In this work, PDMS was chosen as a polymer matrix to embed WO_3 nanoparticles on tapered optical fiber. The polymer composite also serves to protect the tapered fiber from environmental perturbations and increase the mechanical strength of the tapered region. WO_3/PDMS nanocomposite tapered fiber SAs have been employed in ring cavity of 1.56 μm [46] and 1.95 μm [47] and achieved 800 fs and 1.26 ps pulse duration in CS regime, respectively. It has also been reported to generate NLP in the L-band with 10 nJ wave packet energy under 3.5 W pump power [48]. Nevertheless, these reported works only demonstrated single operation state of ultrashort pulses. The aptness of switching operation states from one to another in a single fiber laser cavity would be beneficial for multiple applications or for an application that is multifunctional. Fundamentally, switching between different operation states of ultrashort pulse can be made possible by the nonlinear absorption and RSA effects. Therefore, the primary objective of this work is to extend the investigation on WO_3 based SA for the generation of mode-locked pulses and as a switcher between operation states. A WO_3/PDMS spin-coated tapered fiber was fabricated and had nonlinear parameters of 8.50% MD and 440.08 MW/cm^2 I_{sat} at 1,560 nm wavelength. The fabricated WO_3/PDMS-SA was able to form both CS and NLP in a single cavity of net negative dispersion simply by tailoring the pump power without birefringence feedback. The CS regime began at 82.5 mW while the switch to NLP regime was attained at pump power of 213.2 mW due to the RSA and soliton collapse effect. This is an improvement to previously reported work on WO_3 where the NLP was achieved with pump power greater than 300 mW. The pulse performance of both regimes presents excellent stability. This work contributes to the practicality of WO_3 nanoparticles in attaining various pulse phenomena with different competitive advantages for diverse potential applications in the future.

2 Experimental section

2.1 Preparation of WO_3/PDMS-SA

The fabrication of the SA can be divided into four stages, schematically illustrated in Figure 1. The experiment begins with the preparation of WO_3 nanoparticles. Unlike other techniques of producing nanoparticles *via* various chemical reactions [49], probe-sonication of commercially available bulk WO_3 was employed in this work. In the experiment, 5 mg of bulk WO_3 was weighed and placed into a glass tube containing 10 mL of isopropanol (IPA). After 12 h of sonication process, a well-dispersed WO_3/IPA solution was attained (Figure 1(a)). To prepare a WO_3/PDMS nanocomposite (Figure 1(b)), 2 g of PDMS prepolymer was added into the WO_3/IPA solution, and the mixture was continuously stirred overnight at 70°C to evaporate the IPA, which yielded WO_3/PDMS nanocomposite as the product. A curing agent was introduced in 10:1 ratio of prepolymer to curing agent and stirred for another 10 min to homogenize the nanocomposite. The nanocomposite was subsequently placed inside a vacuum chamber for degassing process.

Afterward, a tapered fiber was fabricated using a commercial fiber tapering machine (Vytran GPX-3400) for WO_3/PDMS nanocomposite deposition (Figure 1(c)). A section of SMF was stripped of its polymer coating layer so that its cladding section was exposed. The stripped section was then heated by a 50 W filament while the ends of the fiber were simultaneously pulled at 1.0 mm/s velocity to produce the desired tapered fiber. A tapered fiber is composed of several sections as illustrated in Figure 1(c); down-tapered (A), waist (B), and up-tapered (C) regions. At the waist region, its diameter is denoted as (D) region. Based on an adiabatic tapered fiber design where the tapering angle, θ should be less than 5 mrad [50], the taper dimensions were 20, 0.5, 20 mm, and 10 μm from region A to D, respectively. An adiabatic tapered fiber minimizes optical loss while preserving the evanescent strength around the tapered region. The tapered fiber was locked on the deposition platform using scotch tape on its ends. The as-prepared WO_3/PDMS

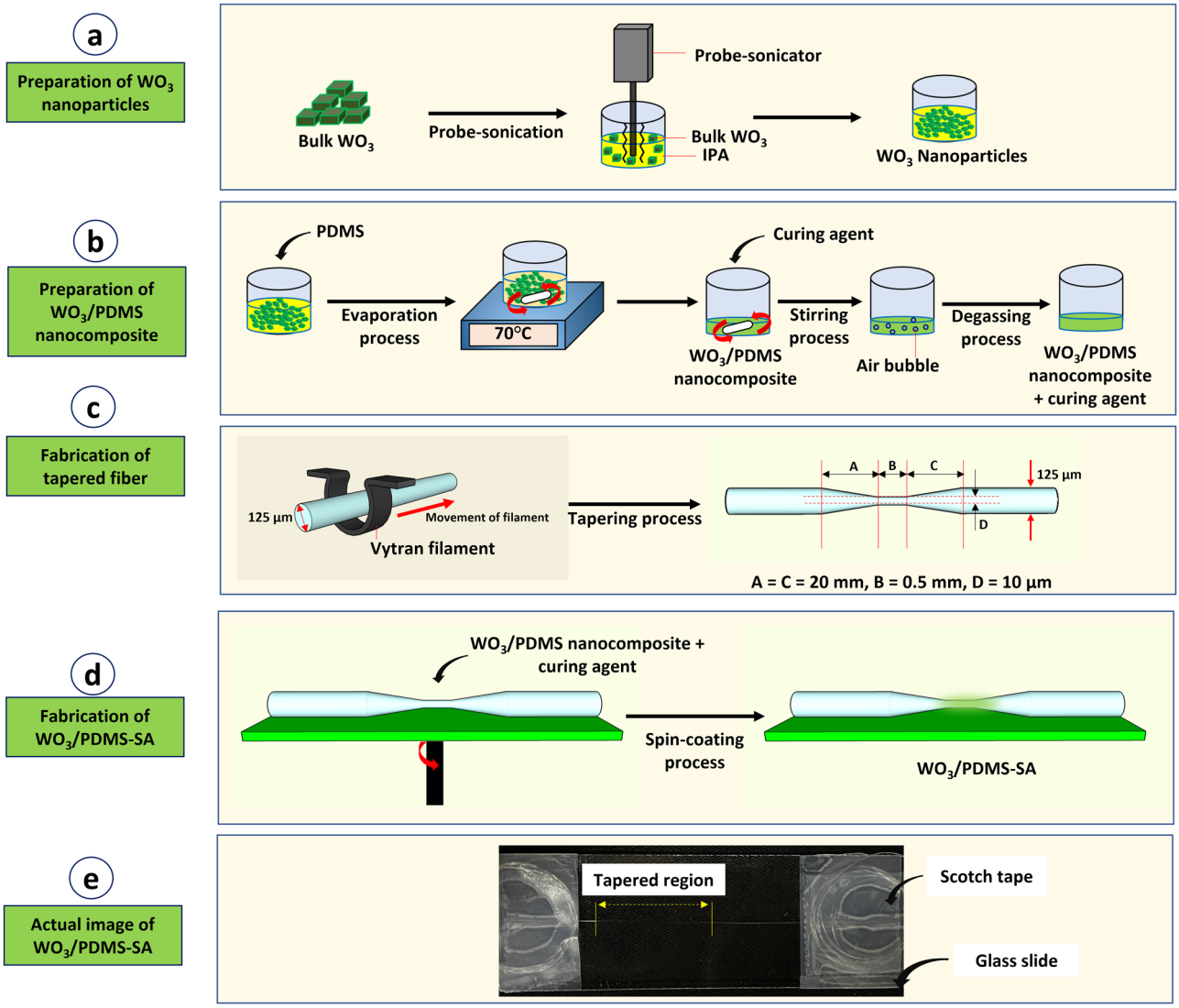

Figure 1: (a)–(d) Methodology of WO_3/PDMS-SA fabrication and (e) aectual image of WO_3/PDMS-SA on glass slide.

nanocomposite was dropped on the tapered region and spin-coated at a speed of 4,000 rotations per minute for 5 min as depicted in Figure 1(d). Finally, the WO_3/PDMS-SA was allowed to solidify at ambient environment for a week. Figure 1(e) shows the actual image of the fabricated WO_3/PDMS-SA after it had been cured.

2.2 Material and SA characterizations

The effect of probe-sonication process on the morphology of WO_3 was conducted using JEOL JSM-6700F field emission scanning electron microscopy (FESEM). In terms of linear optical characteristic of WO_3 nanoparticles, the bandgap energy was characterized using Shimadzu UV-3600 ultraviolet–visible spectroscopy. For the linear transmission characterization of the prepared WO_3/PDMS-SA, an amplified spontaneous emission source was injected into the SA and the transmission spectrum was acquired using a Yokogawa AQ6370B optical spectrum analyzer, as shown in Figure 2(a). Following that, the nonlinear saturable transmittance performance of the prepared WO_3/PDMS-SA was characterized with a standard balanced twin-detector measurement setup as illustrated in Figure 2(b). The setup was pumped with Laser-Femto pulse laser source (PLS) with central wavelength of 1,560 nm, pulse duration of 150 fs, and repetition rate of 60 MHz. The PLS was used as the incident pulse where its intensity was manipulated using an attenuator. The propagating light was split into two optical paths *via* a 3 dB optical coupler (OC), where half of the light power was delivered into the WO_3/PDMS-SA while the other half served as reference power. A pair of Thorlabs PM100D optical power meters coupled with S146C thermal sensors were used to record

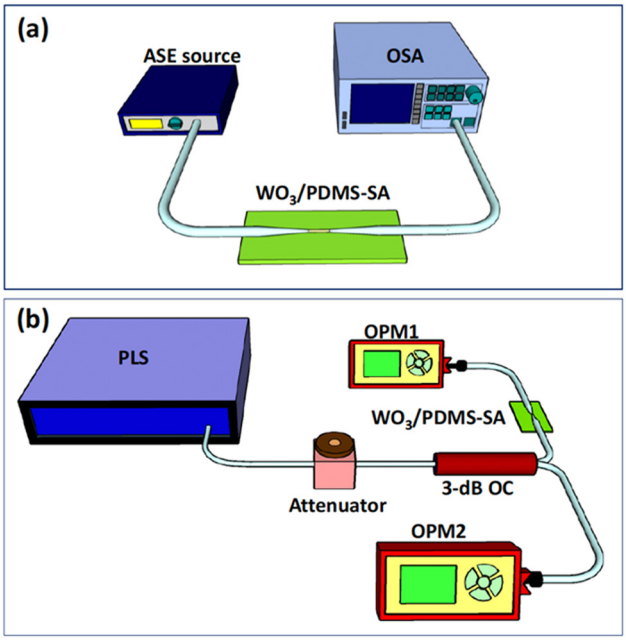

Figure 2: (a) Linear and (b) nonlinear transmission measurements of WO_3/PDMS-SA.

the power-dependent nonlinear transmission of the WO_3/PDMS-SA. The fitting of the experimental transmission data *versus* intensity curve to equation (1) follows the simplified two-level SA model and retrieved three independent parameters, which are MD, non-saturable loss (T_{ns}), saturation intensity (I_{sat}), and TPA coefficient (β), while $T(I)$ denotes transmittance at a particular incident intensity as follows:

$$T(I) = 1 - \mathrm{MD} \times e^{\frac{-I}{I_{sat}}} - T_{ns} - \beta I. \quad (1)$$

2.3 Configuration of mode-locked fiber laser

The configuration of the MLFL cavity with WO_3/PDMS-SA is depicted in Figure 3. A 980 nm laser diode was employed to pump EDF *via* 1 m length of Hi-1060 SMF of the common port at wavelength division multiplexer. The length of the employed EDF was 7.8 m with a core diameter of 5 µm, 200 ppm Er^{3+} concentration and 3.5 dB/m absorption at 1,530 nm for a central wavelength lasing between 1,550 and 1,560 nm. The MLFL cavity was designed to have unidirectional signal propagation by incorporating a polarization insensitive isolator (ISO). A polarization controller (PC) composed of three paddles wrapped with fiber was deployed mainly to determine the polarization-dependent characteristics of the cavity before the integration of SA and to optimize the intracavity birefringence after the SA integration. An 80/20 OC was employed to guide 20% of the output for laser measurement and 80% of the propagating light coupled back into the cavity to complete the ring laser configuration. The total cavity length was 21.50 m, where the remaining length was SMF-28 from the optical components was used to build the cavity. The values of dispersion coefficient (β_2) are 23, –7, and –22 ps^2/km for EDF, Hi-1060 SMF, and SMF-28, respectively. This yielded a net negative GVD of –0.1069 ps^2, permitting the laser to operate in the anomalous dispersion regime.

The optical domain of the MLFL was recorded using an optical spectrum analyzer (OSA, Yokogawa AQ6370B) with resolution bandwidth of 0.02 nm. The output powers were measured using an optical power meter (Thorlabs, PM100D) through a thermal sensor (Thorlabs S302C). The time and frequency domain traces of the generated pulses were measured using 100 MHz digital phosphor oscilloscope (Tektronik TDS 3012C) and electrical spectrum analyzer (GW Instek GSP), respectively, *via* a 5 GHz InGaAs-biased detector (Thorlabs, DET08CFC) photodetector. The radio and video bandwidth resolution were set at 30 and 30 kHz, respectively. Finally, the optical pulse width was characterized using an autocorrelator (A.P.E. PulseCheck).

Before the SA integration to the ring laser cavity, a preliminary test was performed by tuning the PC at all possible polarization states from the lowest pump power up to the maximum pump power of 317.7 mW. The results of the preliminary test demonstrated that the laser operated in continuous wave (CW) mode without self-pulsing which verified that the optical components did not

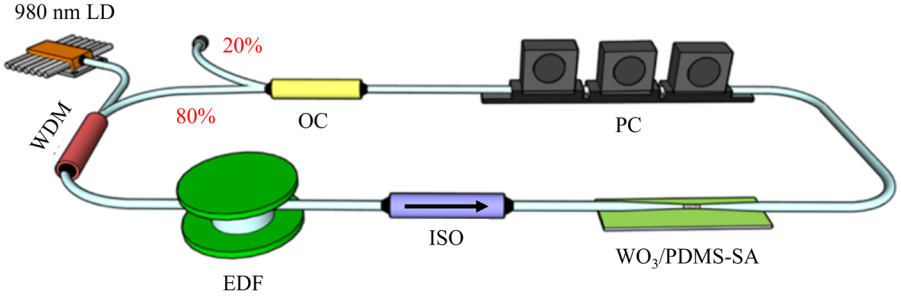

Figure 3: Schematic diagram of the WO_3/PDMS-SA integrated MLFL cavity.

contribute to any mode-locking operation. This test also confirmed that mode-locking achieved after SA integration was not initiated by NPR. Subsequently, the fabricated WO_3/PDMS-SA was spliced between the ISO and PC in the laser cavity to assemble all-fiber MLFL cavity.

3 Results and discussion

3.1 Material and SA characterizations

The morphologies of the bulk and sonicated WO_3 are shown side by side in Figure 4(a) and (b), respectively. After undergoing probe-sonication, the bulk WO_3 with an average size of 37.44 ± 8.81 nm disintegrated into nano-sized particles of 104.21 ± 27.89 nm, which were carefully measured as shown in the histogram of Figure 4(c). The nanoparticles were irregular in shape with square edges, resembling polygons [51]. The purity of the sample was further examined using EDX analysis as presented in Figure 4(d) showing high percentage of tungsten (W) and oxygen (O), while carbon (C) originated from the carbon tape utilized during sample characterization. Therefore, the successful endeavor to generate nanoparticles without engaging sophisticated techniques is demonstrated by these micrograph images. Next, the plot of $(\alpha h\nu)^{1/2}$ *versus* photon energy presented in Figure 4(e) reveals a bandgap energy of 2.80 eV, estimated by extrapolating the graph at $(\alpha h\nu)^{1/2} = 0$. This value matches well with previous literature

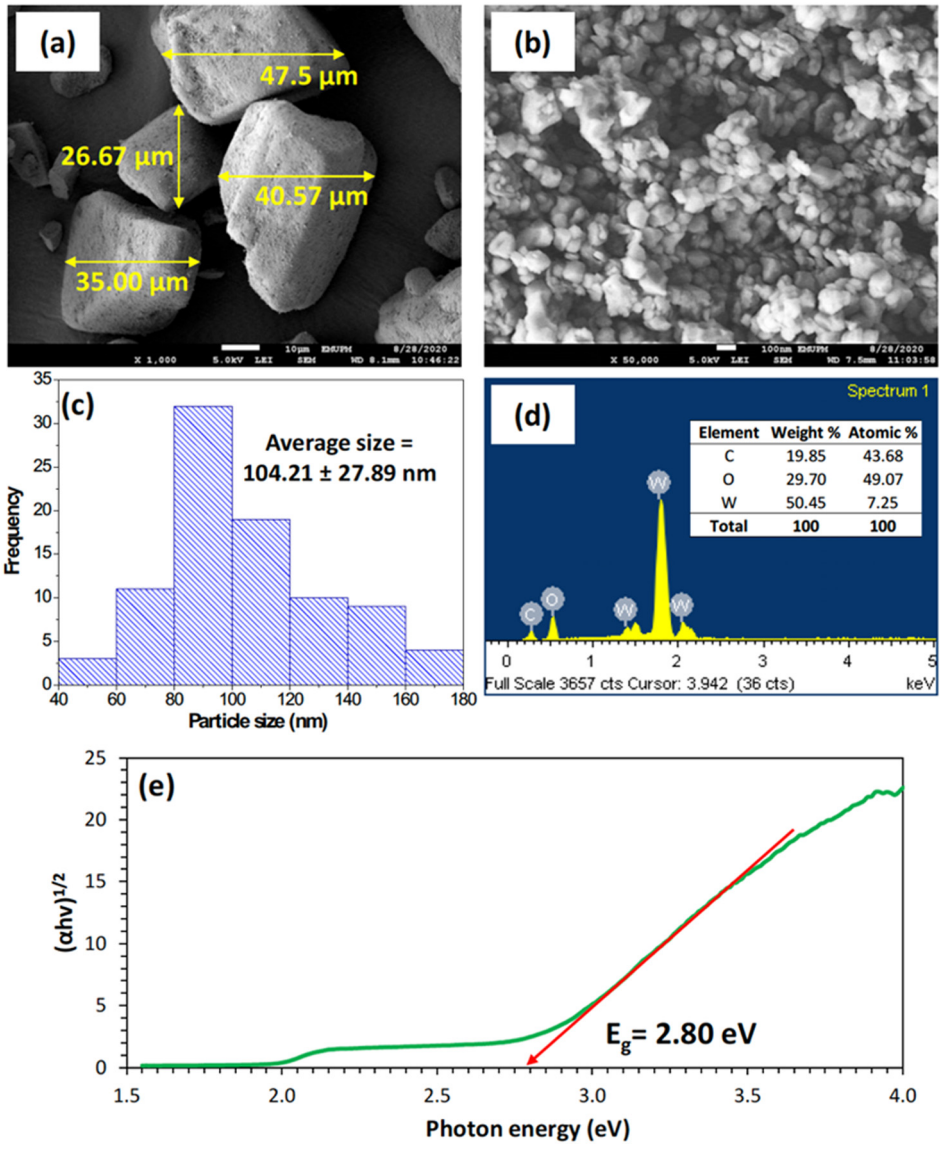

Figure 4: FESEM image of (a) bulk and (b) nanoparticles WO_3, (c) particle size distribution, (d) EDX spectrum, and (e) plot of $(\alpha h\nu)^{1/2}$ *versus* photon energy.

in ref. [52], which is slightly higher than the bandgap of bulk WO_3 (2.54 eV) [53] owing to quantum confinement effect in nano-sized particles. Despite operating at a photon energy lower than the bandgap energy (0.79 eV *vs* 2.80 eV), WO_3/PDMS displays nonlinear saturable characteristic possibly due to edge-state effect which allows for sub-bandgap absorption [54–57]. Figure 5(a) depicts the linear transmission of bare-tapered fiber, PDMS-coated tapered fiber, and WO_3/PDMS-SA which are 93.00, 54.62, and 44.03% at 1,560 nm wavelength, respectively. These transmissions correspond to insertion losses of 0.32, 2.63, and 3.56 dB, respectively. Meanwhile, the presence of WO_3 in nanocomposite coating enhanced the absorption and scattering effect, which resulted in the further decrement in its linear transmittance.

Figure 5(b) presents the nonlinear transmission curve of the WO_3/PDMS-SA, fitted using equation (1). As shown in the figure, the WO_3/PDMS-SA exhibited 8.50% MD, 440.08 MW/cm^2 I_{sat}, and 56.50% T_{ns}. At higher intensity, gradual depletion of the transmission was observed evident of RSA effect. The obvious reduction of transmission at high intensity is commonly addressed as optical limiting behavior experienced by nonlinear materials, which can be due to TPA and enhanced scattering losses under intense laser beam [58] where these effects are responsible for NLP generations [59]. In this work, the value of TPA coefficient (β) was estimated to be 0.0069 cm^2/MW.

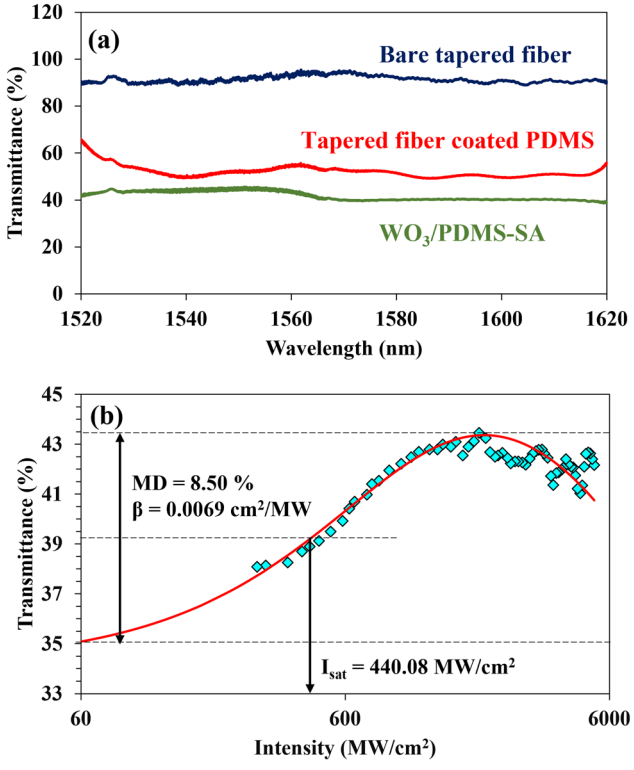

Figure 5: (a) Linear transmission of bare-tapered fiber, PDMS-coated tapered fiber, and WO_3/PDMS-SA. (b) Nonlinear transmission curve of WO_3/PDMS-SA.

3.2 Pulse fiber laser performance

Figure 6(a) shows the optical spectral development of the MLFL at varying pump powers. Initially, CW emission was observed at pump power of 22.8 up until 75.2 mW, followed by self-starting mode-locked operation at 82.5 mW as presented in Figure 6(a). The mode-locked generation operated in CS regime by the simultaneous generation of Kelly sidebands on the spectral envelope, which occurred as a consequence of constructive interference between solitons and dispersive waves with a phase difference of 2π-multiples. The presence of these sidebands implies that the accumulated phase difference acquired by propagating solitons is nearly orthogonal to dispersive waves. As a result, dispersive waves are filtered by orthogonally polarized components while solitons pass through, disarraying the phase-matching condition for sideband generation [60]. The Kelly sidebands were maintained up to 181.3 mW pump power. In Figure 6(b), the mode-locked generation became unstable at pump power of 187.9 mW before a complete suppression of the stochastic spectral components accompanied with abrupt broadening effect of the spectral envelope at 213.2 mW. The enhancement of 3 dB bandwidth from 6.72 to 16.47 nm supports the narrative of a pulse transition regime from CS to NLP. The smooth optical spectrum continued to broaden steadily up to the maximum pump power of 288.6 mW, positioned at 1557.31 nm with bandwidth of 17.98 nm. Figure 6(c) shows the average output power and pulse energy of CS and NLP against pump power. It is observed that the average output power and pulse energy grow linearly with the increase of pump power. The maximum average output power in the CS regime is 3.67 mW at 181.3 mW, corresponding to a pulse energy of 0.403 nJ. CS pulse energy is typically predicted to be less than 0.1 nJ based on the soliton theorem, but it has been experimentally demonstrated in several investigations that the pulse energy of solitons in net anomalous dispersion cavity could exceed the stipulated value due to smaller net negative dispersion induced by self-phase modulation at higher pump powers [61] In the NLP regime, the maximum average output power is 5.49 mW at 288.6 mW pump power, while the pulse energy is 0.604 nJ.

The pulse train of the MLFL has a pulse separation of 110.0 ns which reciprocates to a fundamental repetition

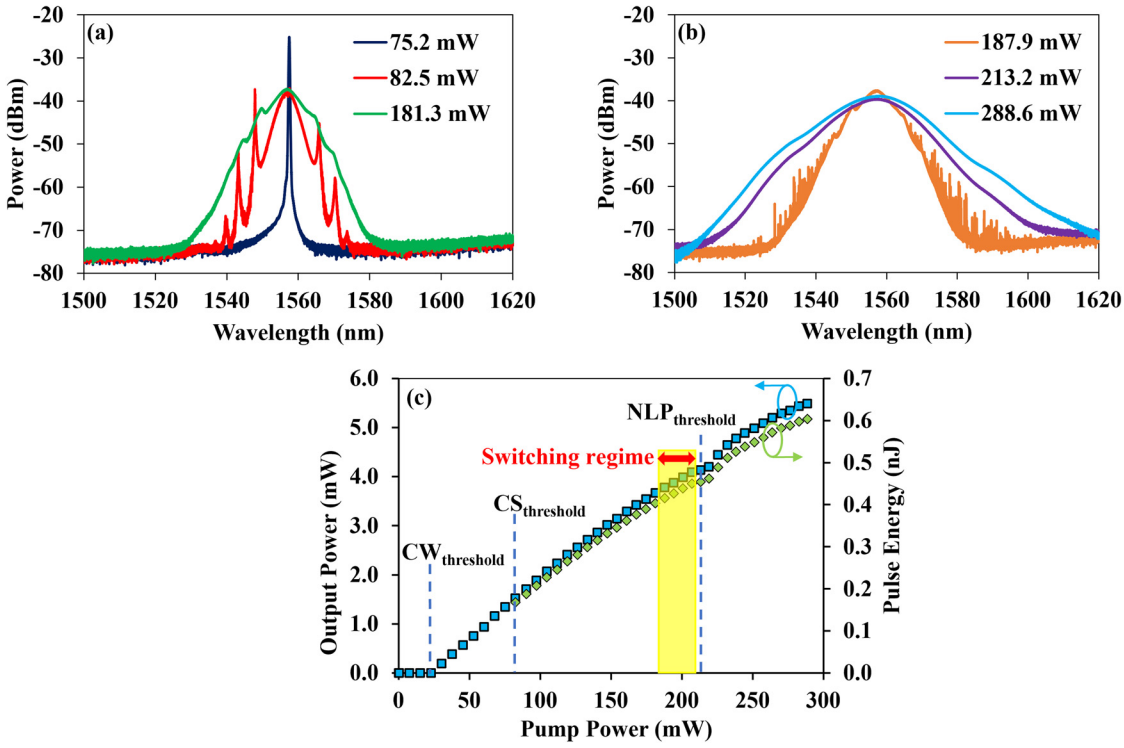

Figure 6: (a) and (b) Optical spectrum and (c) power and pulse energy evolution of the MLFL based on WO_3/PDMS-SA.

rate of 9.09 MHz as shown in Figure 7. The pulse trace of CS shows excellent stability at 181.3 mW pump power presented as a stable envelope state in the longer time range, as shown in the inset of Figure 7(a). During the switching regime at 187.9 mW, the pulse separation remains at 110 ns as shown in Figure 7(b) but exhibits instability from the obvious voltage fluctuation in the long-time range trace (inset). In the NLP regime taken at 288.6 mW, a stable state of pulse train was observed as shown in Figure 7(c). Despite the complex dynamics of massive sub-pulses within a wave packet in NLP regime, it propagates as a single unit in the cavity at the fundamental repetition frequency which appears invariable to the CS regime in the oscilloscope [62]. To validate the switching regime of CS to NLP, the autocorrelation traces were measured and analyzed. As illustrated in Figure 8(a), the CS regime delivers a pedestal-free pulse profile captured at 181.3 mW pump power with 970.0 fs duration width assuming a $Sech^2$ pulse profile. The time bandwidth product (TBP) is 0.806 compared to the transform-limited value of 0.314 indicating that the pulses are chirped. Increasing the pump power beyond 187.9 mW, the autocorrelation trace exhibited pulse width narrowing as shown in Figure 8(b) alongside the increase in pulse energy (Figure 6(c)). This translates to high peak power condition possibly triggering RSA. In the succession of triggered RSA, the switching regime between CS and NLP takes place manifesting as instability and unfitted trace. The existence of RSA in WO_3 nanoparticles of 100 nm average sizes has been reported in ref. [63]. Further increasing the pump power to 288.6 mW, the autocorrelation traces taken at short span of 4 ps and long span of 120 ps show distinct feature of NLP with a 182.0 fs coherent spike upon a 65.3 ps broad pedestal as depicted in Figure 8(c) confirming the operation switch. In the NLP regime, the estimated TBP is 0.450 which is approximately the transform-limited value for Gaussian pulses of 0.441. In this regime, the maximum pulse energy achieved is 0.604 nJ at 281 pump power, a 50% percent increase to CS.

The measurements of the RF spectrum, signal-to-noise ratio (SNR) at maximum pump power are shown in Figure 9. The SNR acquired at the fundamental repetition rate of 9.09 MHz for CS regime was 50.76 dB as depicted in Figures 9(a), and 49.82 dB at NLP regime as shown in Figure 9(c), indicating a reasonably stable laser operation. This is comparable to the previous work in ref. [37]. In the switching regime, Figure 9(b) shows uneven RF peaks between pump powers 187.9 and 207.1 mW despite matching the repetition rate of the cavity corroborating the instability observed earlier in the autocorrelation trace (Figure 8(b)). To confirm the stability of the mode-locked laser in CS and NLP regime, the optical spectrum was measured during an observation period

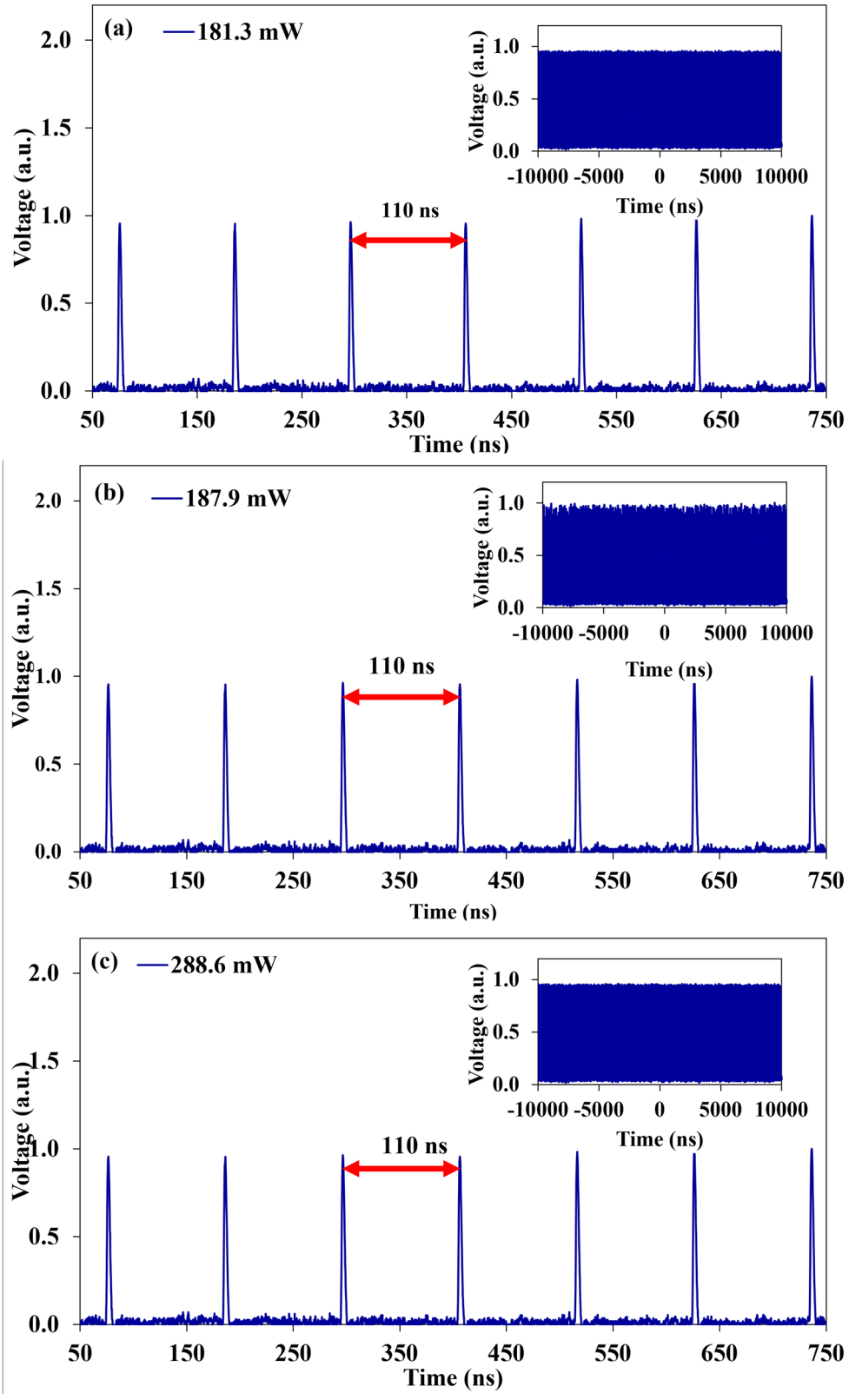

Figure 7: Oscilloscope trace at (a) CS regime, (b) switching regime, and (c) NLP regime (insets: oscilloscope trace in long time range).

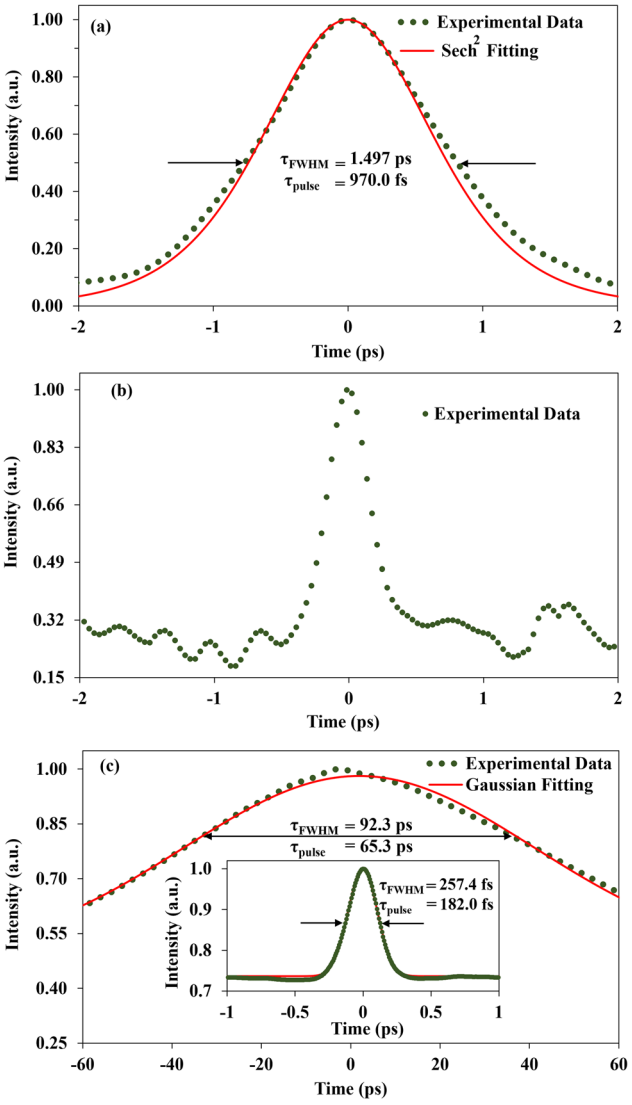

Figure 8: Autocorrelation trace at (a) CS regime, (b) switching regime, and (c) NLP regime.

of 60 min at2 min intervals as portrayed in Figure 10. The measurements were all performed at the maximum pump power of CS (181.3 mW) and NLP regime (288.6 mW). Based on the experimental findings, the average values for the central wavelength and 3 dB spectral bandwidth at CS regime were determined to be 1556.64 ± 0.03 and 6.67 ± 0.16 nm, respectively. For NLP regime, the central wavelength and 3 dB spectral bandwidth values were analyzed to be 1557.48 ± 0.06 and 17.89 ± 0.36 nm, respectively. Both regimes show excellent mode-locked stability.

Comparison of different tapered fiber-based 2D material-SAs for multiple operation states of ultrashort pulse fiber laser.

Figure 11 summarizes the nanomaterial decorated tapered fiber as mode-locker. Wang *et al.* fabricated bismuthene-SA *via* simple drop-casting technique [64]. However, the main disadvantage of this method is poor material attachment onto the taper waist, as evidenced by its small MD of 2.4% [64]. Optical deposition, on the other hand, uses optical trapping effect induced by injected light offers a solution for earlier method with higher probability of material attachment and excellent nonlinear properties [65]. It should be noted that this technique is best used with two-dimensional or nano-sized material due to their flexibility to attach and stack onto the substrate compared to bulk sizes. For instance, the MD in refs [16,18,41,66–68] varies from 4.4 to 27.89%, depending on the deposition time, injected power, taper waist diameter, type of solvent used, and size of nanomaterials. However, the SA device might have a short shelf-life if there is neither an encapsulating agent nor packaging. Therefore, the inclusion of polymer in SA fabrication assists in securing the attached material while providing mechanical support to the fragile tapered fiber. A low refractive index polymer like PDMS has been frequently used in SA fabrication due to its hydrophobic property and high viscosity [46,47]. In this work, the indirect and weak evanescent-wave coupling of the embedded WO_3/PDMS yielded highest I_{sat} of 440.08 MW/cm^2 and moderate MD of 8.5%, which is relatively higher than [16,18,64,68] and significantly lower than the work in refs [41,66,67].

Figure 12(a) and (b) summarizes the pulse performance of CS regime, wherein $W_xNb_{(1-x)}Se_2$ in ref. [68] demonstrated nearly transform-limited pulse of 131 fs with broad 3 dB spectral bandwidth of 23 nm. Despite its short cavity length, the large power extraction and high pump power successfully produced single pulse energy of 0.81 nJ [68]. The strategy of short cavity length for ultrafast pulse width was also practiced in other works: $Re_xNb_{(1-x)}S_2$ [67], bismuthene [64], and manganese dioxide (MnO_2) [16], with pulse widths of 285, 622, and 850 fs, respectively. However, this kind of cavity design suffers from high mode-locking threshold condition due to the insufficient intracavity nonlinearity. In CS regime, a fair comparison can be made between this work and Graphdiyne in ref. [66] due to the almost similar cavity length. Although Graphdiyne reported high output power (8.4 mW) and pulse energy (0.93 nJ), the CS pulse width (2.21 ps) was far slower than this work (970 fs). As depicted in Figure 12(c), the attained CS pulse energy in this work was 0.4 nJ, while higher pulse energy could be achieved by lengthening the cavity length [41], using a higher coupling ratio at the output [68], or pumping the laser cavity with higher pump power [41,66,68] provided that the MD is sufficiently high to mitigate the pulse breaking effect.

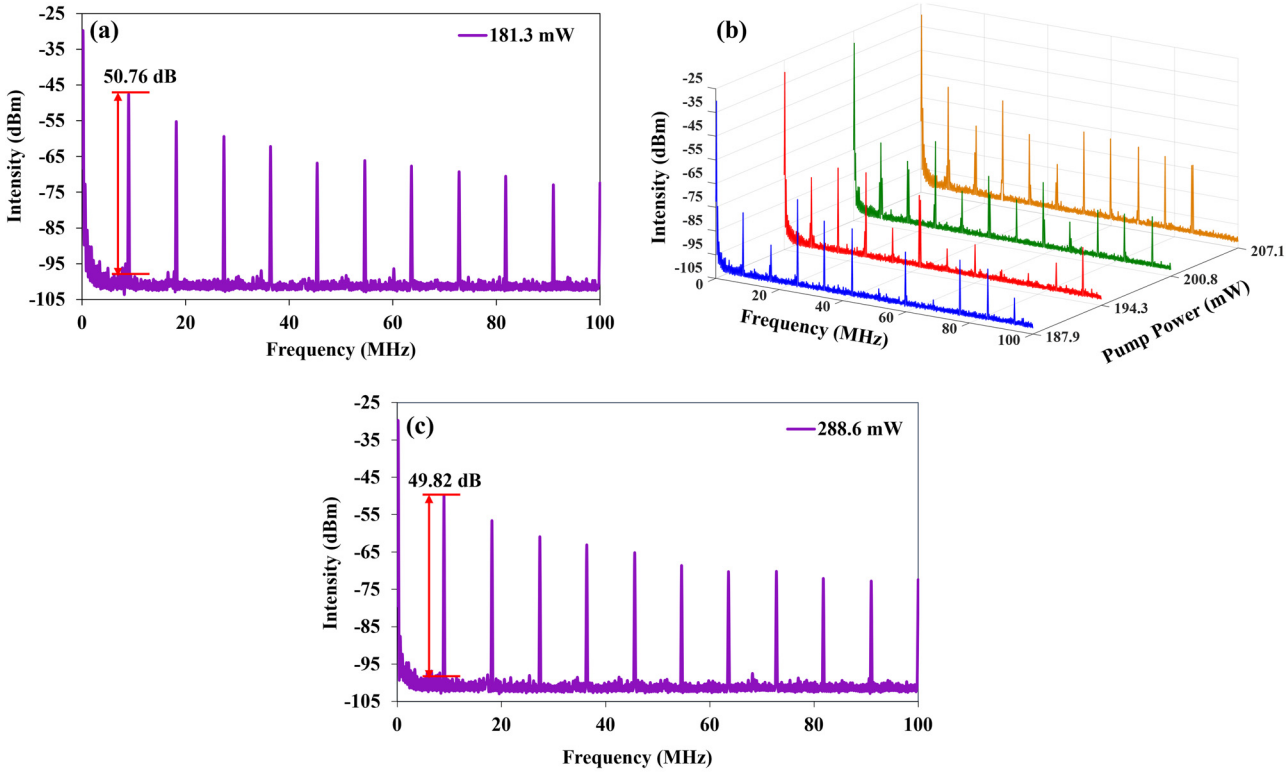

Figure 9: The RF spectrum at (a) CS regime, (b) switching regime, and (c) NLP regime.

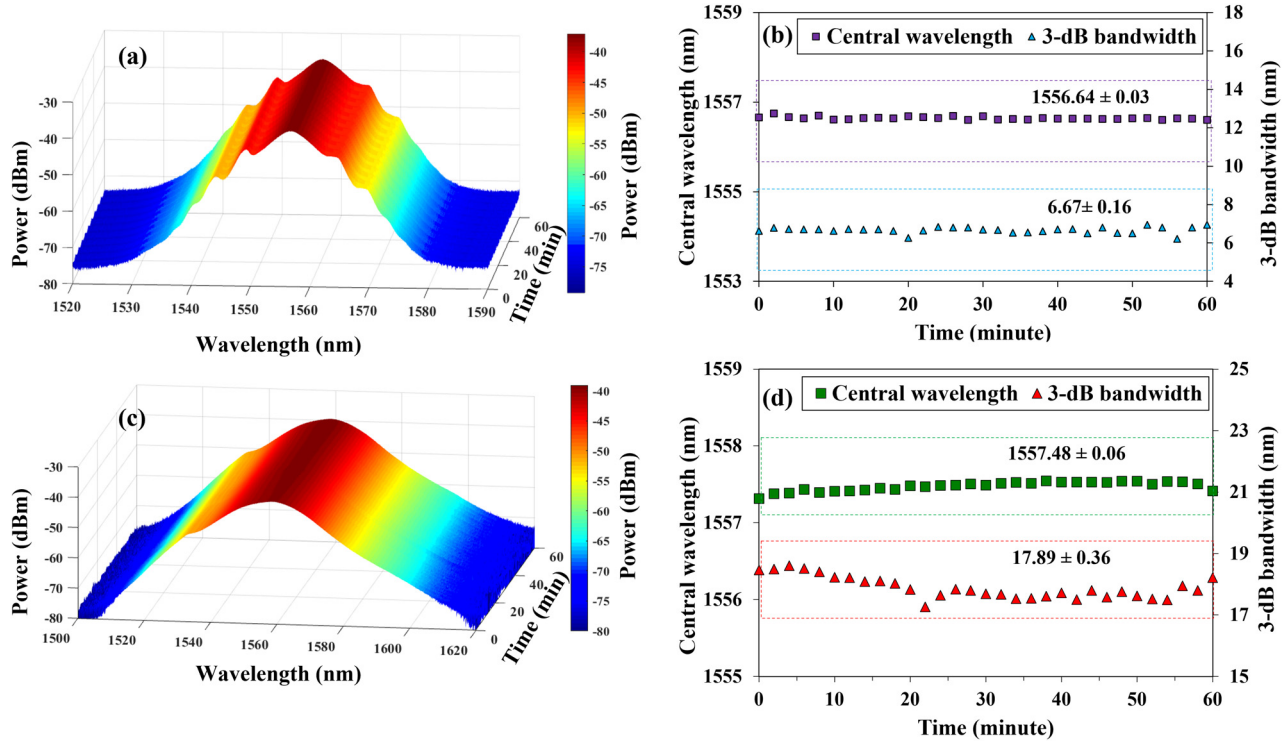

Figure 10: Stability test performance at 181.3 mW for the CS regime: (a) optical spectrum, (b) central wavelength and 3 dB spectral bandwidth, and at 288.6 mW for the NLP regime, (c) optical spectrum, and (d) central wavelength and 3 dB spectral bandwidth.

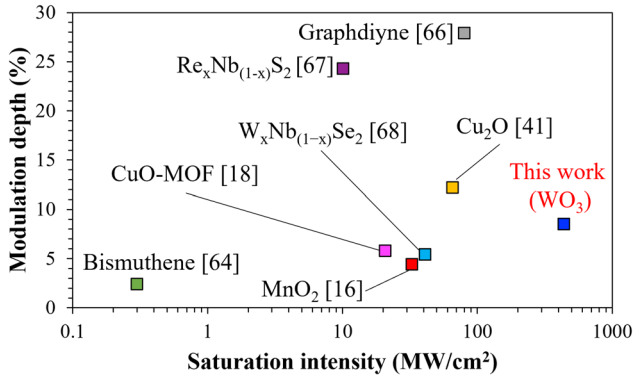

Figure 11: MD against saturation intensity of tapered fiber-based SAs.

Figure 12(c) presents various pulse dynamics with respect to pump powers, whereas their pulse energy at maximum pump powers is portrayed in Figure 12(d). The pulse splitting effect is frequently observed when the intracavity peak power exceeds a certain level. For instance, harmonic mode-locking is recognized by the multiplication of fundamental frequency with an integer, and the adjacent pulses are evenly spaced to each other, as reported by Li and associates with 251th harmonics [41]. Besides that, bound soliton in harmonic mode-locking state was also reported in several works [16,18,67], whereby it can be easily identified by observing spectral modulation in optical domain and co-existence of sub-pulses in time domain. Other multiple pulse that travels with fundamental frequency, dubbed as NLP can be easily attained due to soliton collapse effect, high pumping condition, and presence of TPA and RSA in the laser cavity. In Figure 12(d), the summary of pulse energy at maximum pump power for different pulse dynamics is plotted. The pulse energy of NLP in this work is higher than $Re_xNb_{(1-x)}S_2$ (0.39 nJ) [67] and bismuthene (0.48 nJ) [64], and significantly lower than graphdiyne (2.17 nJ) [66]. Even higher pulse energy (257 nJ) was reported by Li and co-workers [68] with $W_xNb_{(1-x)}Se_2$ *via* Q-switching technique. However, the main drawback of Q-switched pulse is the slow pulse width within microsecond duration, limited by the material's recovery time.

From the results shown thus far, by increasing the pump power, the spectral bandwidth of CS becomes comparable to the gain bandwidth of erbium. TPA and roll-off effect of saturable absorption are stimulated in the fabricated WO_3/PDMS-SA, giving rise to a soliton collapse effect and NLP emission that repeats at the fundamental cavity repetition rate [69,70]. As a result, the MLFL exhibited (1) an optical spectrum with Kelly's sidebands evolved to a very broad and smooth optical spectrum, (2) a fair SNR in the RF spectrum, and (3) a $Sech^2$ pulse profile with no pedestal that transformed to a narrow Gaussian-fitted

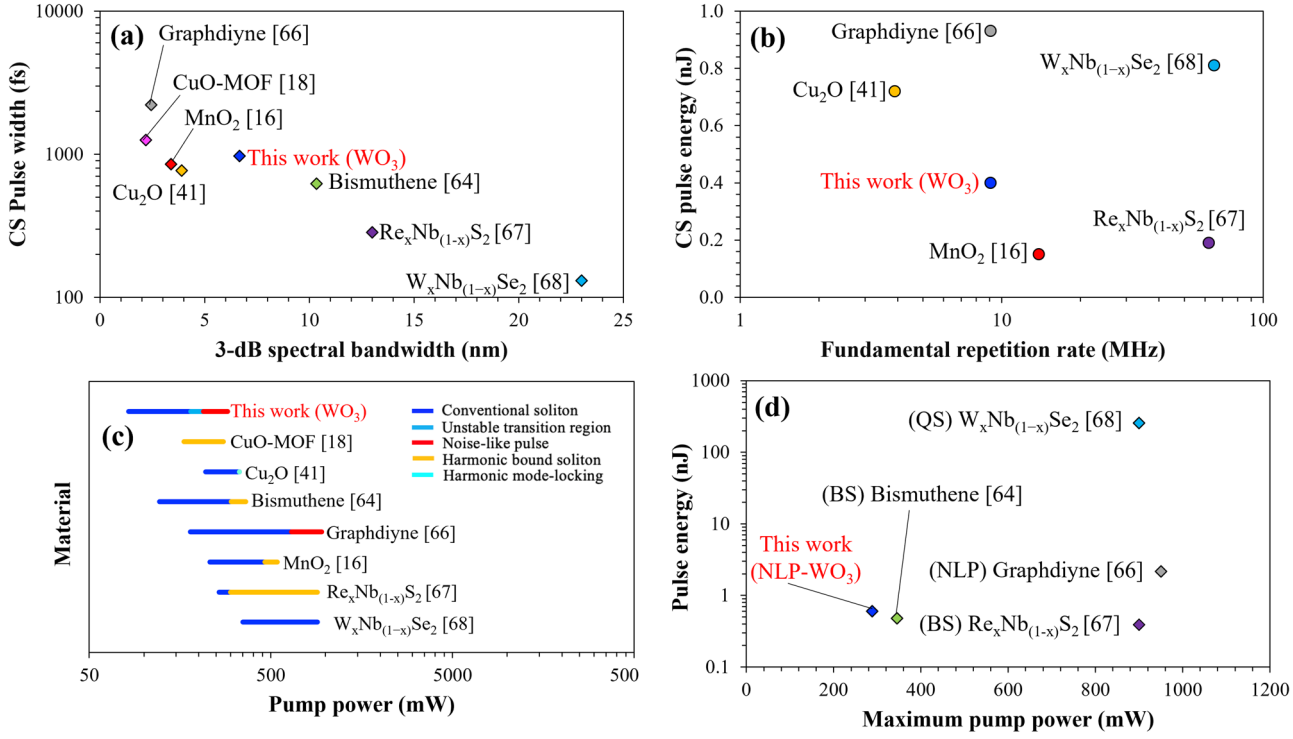

Figure 12: Critical reviews on tapered fiber-based SAs for various pulse dynamics: (a) CS pulse width *versus* 3 dB spectral bandwidth, (b) CS pulse energy *versus* fundamental repetition rate, (c) pulse dynamics against pump powers, and (d) pulse energy at maximum pump powers.

coherent pulse overlapped with a broad pedestal containing a group of pulse with random fine structures that holds together as one pulse envelope. The soliton collapse effect triggered by TPA and RSA presented instability in the form of random densely packed components on the spectral envelope (Figure 6(b)), unfitted narrowing AC trace, and uneven RF peaks. In a previous work, it has also been experimentally proven that nano-sized WO_3 particles are capable to exhibit such multi-photon absorption which was characterized using intensity dependent z-scan method [71]. Moreover, to avoid soliton collapse and to ensure that only fundamental pulses circulate inside the laser cavity at wide pump power range, a SA with higher MD and critical power of TPA is favorable.

4 Conclusion

In this work, we successfully demonstrated a MLFL operating in anomalous dispersion regime by employing WO_3/PDMS deposited on a tapered fiber as SA. The MLFL features the switching of CS to NLP by pump power manipulation in a common fiber cavity without birefringence feedback, where the critical power threshold of realizing NLP was at 213.2 mW. In the CS regime, a chirped pulse of 970.0 fs duration with 0.4 nJ pulse energy and spectral 3 dB bandwidth of 6.72 nm was achieved. A drastic enhancement of 3 dB bandwidth to 16.47 nm was observed when the CS pulse collapsed into the NLP with a clear autocorrelation trace of 182.0 fs imposed on a broad 65.3 ps pedestal. At the pump power of 288.6 mW, the broadest optical spectrum of 17.98 nm positioned at 1557.91 nm central wavelength was accomplished. The MLFL showed good laser performance and stability with small standard deviations, with 50.76 dB SNR in the CS regime and 49.82 dB in the NLP regime at a constant fundamental repetition rate of 9.09 MHz. The versatility of this simple MLFL escalates potential for a compact dual-purpose laser system.

Funding information: This work was supported by the Collaborative Research in Engineering, Science and Technology (CREST), Malaysia under the Open R&D Grant (P07C1-19) and King Saud University, Kingdom of Saudi Arabia under the Researchers Supporting Project (RSP2023R336)

Author contributions: All authors have accepted responsibility for the entire content of this manuscript and approved its submission.

Conflict of interest: The authors state no conflict of interest.

References

[1] Gong Q, Zhao W. Ultrafast science to capture ultrafast motions. Ultrafast Sci. 2021;2021:9765859.
[2] Xiao Y, Feng C, Liu B. Generating isolated attosecond X-ray pulses by wavefront control in a seeded free-electron laser. Ultrafast Sci. 2022;2022:9812478.
[3] Mustary MH, Xu L, Wu W, Haram N, Laban DE, Xu H, et al. Attosecond delays of high-harmonic emissions from hydrogen isotopes measured by XUV interferometer. Ultrafast Sci. 2022;2022:9834102.
[4] Hu M, Zheng Y, Yang Y, Chen X, Liu K, Zhao C, et al. Nanosecond double-pulse fiber laser with arbitrary sub-pulse combined based on a spectral beam combining system. Opt Laser Technol. 2017;90:22–6.
[5] Lin Z, Hong M. Femtosecond laser precision engineering: from micron, submicron, to nanoscale. Ultrafast Sci. 2021;2021:9783514.
[6] Mamalis N. Femtosecond laser: the future of cataract surgery? J Cataract Refract Surg. 2011;37(7):1177–8.
[7] de Menezes RF, Harvey CM, de Martínez Gerbi ME, Smith Z, Smith D, Ivaldi J, et al. Fs-laser ablation of teeth is temperature limited and provides information about the ablated components. J Biophotonics. 2017;10(10):1292–304.
[8] Smirnov SV, Kobtsev SM, Kukarin SV. Efficiency of non-linear frequency conversion of double-scale pico-femtosecond pulses of passively mode-locked fiber laser. Opt Express. 2014;22(1):1058–64.
[9] Bagheri M, Frez C, Sterczewski LA, Gruidin I, Fradet M, Vurgaftman I, et al. Passively mode-locked interband cascade optical frequency combs. Sci Rep. 2018;8(3322):1–7.
[10] Tozburun S, Blatter C, Siddiqui M, Meijer EFJ, Vakoc BJ. Phase-stable Doppler OCT at 19 MHz using a stretched-pulse mode-locked laser. Biomed Opt Express. 2018;9(3):952–61.
[11] Guo B, Xiao Q, Wang S, Zhang H. 2D layered materials: synthesis, nonlinear optical properties, and device applications. Laser Photonics Rev. 2019;13(12):1800327.
[12] Kutz JN. Mode-locked soliton lasers. SIAM Rev. 2006;48(4):629–78.
[13] Grelu P, Akhmediev N. Dissipative solitons for mode-locked lasers. Nat Photon. 2012;6:84–92.
[14] Xu S, Turnali A, Sander MY. Group-velocity-locked vector solitons and dissipative solitons in a single fiber laser with net-anomalous dispersion. Sci Rep. 2022;12:6841.
[15] Akhmediev N, Soto-Crespo JM, Vouzas P, Devine N, Chang W. Dissipative solitons with extreme spikes in the normal and anomalous dispersion regimes. Philos Trans R Soc. 2018;376(2124):20180023.
[16] Han Y, Li X, Chen E, An M, Song Z, Huang X, et al. Sea-Urchin-MnO_2 for broadband optical modulator. Adv Opt Mater. 2022;10(22):2201034.
[17] Chen Y, Wu M, Tang P, Chen S, Du J, Jiang G, et al. The formation of various multi-soliton patterns and noise-like pulse

in a fiber laser passively mode-locked by a topological insulator based saturable absorber. Laser Phys Lett. 2014;11(5):055101.
[18] Zhao Y, Wang W, Li X, Lu H, Shi Z, Wang Y, et al. Functional porous MOF-derived CuO octahedra for harmonic soliton molecule pulses generation. ACS Photonics. 2020;7(9):2440–7.
[19] Liu X, Yao X, Cui Y. Real-time observation of the buildup of soliton molecules. Phys Rev Lett. 2018;121(2):023905.
[20] Liu X, Pang M. Revealing the buildup dynamics of harmonic mode-locking states in ultrafast lasers. Laser Photonic Rev. 2019;13(9):1800333.
[21] Wang M, Zhao J, Chen Y, Liu M, Ouyang D, Pei J, et al. 10 μJ noise-like pulse generated from all fiberized TM-doped fiber oscillator and amplifier. Opt Express. 2021;29(7):10172–80.
[22] Özgören K, Öktem B, Yilmaz S, Ilday FÖ, Eken K. 83 W, 3.1 MHz, square-shaped, 1 ns-pulsed all-fiber-integrated laser for micromachining. Opt Express. 2011;19(18):17647–52.
[23] Zaytsev A, Lin C-H, You Y-J, Chung C-C, Wang C-L, Pan C-L. Supercontinuum generation by noise-like pulses transmitted through normally dispersive standard single-mode fibers. Opt Express. 2013;21(13):16056–62.
[24] Lin J-H, Liao T-Y, Yang C-Y, Zhang D-G, Yang C-Y, Lee Y-W, et al. Noise-like pulse generation around 1.3-μm based on cascaded Raman scattering. Opt Express. 2020;28(8):12252–61.
[25] Dong Z, Tian J, Li R, Cui Y, Zhang W, Song Y. Conventional soliton and noise-like pulse generated in an Er-doped fiber laser with carbon nanotube saturable absorbers. Appl Sci. 2020;10(16):5536.
[26] Suzuki M, Ganeev RA, Yoneya S, Kuroda H. Generation of broadband noise-like pulse from Yb-doped fiber laser ring cavity. Opt Lett. 2015;40(5):804–7.
[27] Jeon J, Lee J, Lee JH. Numerical study on the minimum modulation depth of a saturable absorber for stable fiber laser mode locking. J Opt Soc Am. 2014;32(1):31–7.
[28] Liu S, Yan F-P, Zhang L-N, Han W-G, Bai Z-Y, Zhou H. Noise-like femtosecond pulse in passively mode-locked Tm-doped NALM-based oscillator with small net anomalous dispersion. J Opt. 2015;18(1):015508.
[29] Avilés AC, Hernández-Escobar E, López-Estopíer R, Bello-Jiménez M, Pottiez O, Ibarra- Escamilla B, et al. The nonlinear optical loop mirror: soliton and noise-like pulse emission in a figure-eight fiber laser. Suppl Rev Mex Fís. 2021;2(1):54–9.
[30] Li W, Yi L, Zheng R, Ni Z, Hu W. Fabrication and application of a graphene polarizer with strong saturable absorption. Photonics Res. 2016;4(2):41–4.
[31] Zhao LM, Tang DY, Wu J, Fu XQ, Wen SC. Noise-like pulse in a gain-guided soliton fiber laser. Opt Express. 2007;15(5):2145–50.
[32] Tang DY, Zhao LM, Zhao B. Soliton collapse and bunched noise-like pulse generation in a passively mode-locked fiber ring laser. Opt Express. 2005;13(7):2289–94.
[33] Horowitz M, Barad Y, Silberberg Y. Noiselike pulses with a broadband spectrum generated from an erbium-doped fiber laser. Opt Lett. 1997;22(11):799–801.
[34] Bogusławski J, Soboń G, Zybała R, Sotor J. Towards an optimum saturable absorber for the multi-gigahertz harmonic mode locking of fiber lasers. Photonics Res. 2019;7(9):1094–100.
[35] Dong T, Lin J, Gu C, Yao P, Xu L. Noise-like square pulses in both normal and anomalous dispersion regimes. IEEE Photon J. 2021;13(2):1–8.
[36] Wang Q, Chen T, Li M, Zhang B, Lu Y, Chen KP. All-fiber ultrafast thulium-doped fiber ring laser with dissipative soliton and noise-like output in normal dispersion by single-wall carbon nanotubes. Appl Phys Lett. 2013;103(1):011103.
[37] Sobon G, Sotor J, Przewolka A, Pasternak I, Strupinski W, Abramski K. Amplification of noise-like pulses generated from a graphene-based Tm-doped all-fiber laser. Opt Express. 2016;24(18):20359–64.
[38] Cui Y. Bandwidth-tunable dissipative soliton and noise-like pulse in a normal dispersion fiber laser with a dual-scale saturable absorber. J Opt. 2016;18:105503.
[39] Xu N, Ma P, Fu S, Shang X, Jiang S, Wang S, et al. Tellurene-based saturable absorber to demonstrate large-energy dissipative soliton and noise-like pulse generations. Nanophotonics. 2020;9(9):2783–95.
[40] Wang Z, Wang Z, Liu Y-G, He R, Han S, Wang G, et al. Noise-like pulses generated from a passively mode-locked fiber laser with a WS_2 saturable absorber on microfiber. Laser Phys Lett. 2018;15(8):085103.
[41] Li X, Feng J, Mao W, Yin F, Jiang J. Emerging uniform Cu_2O nanocubes for 251st harmonic ultrashort pulse generation. J Mater Chem C. 2020;8(41):14386–92.
[42] Al-Hiti AS, Al-Masoodi AHH, Harun SW, Yasin M, Wong WR. Tungsten trioxide (WO_3) film absorber for generating soliton mode-locked pulses in erbium laser. Opt Laser Technol. 2020;131:106429.
[43] Liu W, Pang L, Han H, Liu M, Lei M, Fang S, et al. Tungsten disulfide saturable absorbers for 67 fs mode-locked erbium-doped fiber lasers. Opt Express. 2017;25(3):2950–9.
[44] Liu W, Pang L, Han H, Bi K, Lei M, Wei Z. Tungsten disulphide for ultrashort pulse generation in all-fiber lasers. Nanoscale. 2017;9(18):5806–11.
[45] Du J, Wang Q, Jiang G, Xu C, Zhao C, Xiang Y, et al. Ytterbium-doped fiber laser passively mode locked by few-layer molybdenum disulfide (MOS_2) saturable absorber functioned with evanescent field interaction. Sci Rep. 2014;4:6346.
[46] Abdul Hadi MAW, Lau KY, Zainol Abidin NH, Baki SO, Ng EK, Kee LH, et al. Investigation of tungsten trioxide as a saturable absorber for mode-locked generation. Opt Laser Technol. 2020;132:106496.
[47] Ahmed MHM, Khaleel WA, Sadeq SA, Abdul Hadi MAW, Zainol Abidin NH, Mahdi MA. Mode-locked thulium doped fiber laser utilizing tungsten trioxide saturable absorber. Opt Laser Technol. 2021;136:106730.
[48] Abdul Hadi MAW, Lau KY, Mohd Yusoff N, Zainol Abidin NH, Alresheedi MT, Abas AF, et al. Nano-tungsten trioxide saturable absorber for L-band noise-like pulse mode-locked fiber laser. Opt Fiber Technol. 2022;71:102933.
[49] Wu C-M, Naseem S, Chou M-H, Wang J-H, Jian Y-Q. Recent advances in tungsten-oxide-based materials and their applications. Front Mater. 2019;6:49.
[50] Ravets S, Hoffman JE, Kordell PR, Wong-Campos JD, Rolston SL, Orozco LA. Intermodal energy transfer in a tapered optical fiber: optimizing transmission. J Opt Soc Am. 2013;30(11):2361–71.

[51] Liu J, Han S, Li J, Lin J. Modification of tungsten trioxide with ionic liquid for enhanced photocatalytic performance. RSC Adv. 2014;4(71):37556–62.
[52] Vemuri RS, Engelhard MH, Ramana CV. Correlation between surface chemistry, density, and band gap in nanocrystalline WO_3 thin films. ACS Appl Mater Interfaces. 2012;4(3):1371–7.
[53] Boruah PJ, Khanikar RR, Bailung H. Synthesis and characterization of oxygen vacancy induced narrow bandgap tungsten oxide (WO_{3-x}) nanoparticles by plasma discharge in liquid and its photocatalytic activity. Plasma Chem. 2020;40(4):1019–36.
[54] Wang W, Yue W, Liu Z, Shi T, Du J, Leng Y, et al. Ultrafast nonlinear optical response in plasmonic 2D molybdenum oxide nanosheets for mode-locked pulse generation. Adv Opt Mater. 2018;6(17):1700948.
[55] Mao D, Cui X, He Z, Lu H, Zhang W, Wang L, et al. Broadband polarization-insensitive saturable absorption of Fe_2O_3 nanoparticles. Nanoscale. 2018;10(45):21219–24.
[56] Niu K, Sun R, Chen Q, Man B, Zhang H. Passively mode-locked Er-doped fiber laser based on SnS_2 nanosheets as a saturable absorber. Photonics Res. 2018;6(2):72–6.
[57] Ahmad H, Reduan SA, Ali ZA, Ismail MA, Ruslan NE, Lee CSJ, et al. C-band Q-switched fiber laser using titanium dioxide (TiO_2) as saturable absorber. IEEE Photon J. 2016;8(1):1–7.
[58] Chen B, Zhang X, Wu K, Wang H, Wang J, Chen J. Q-switched fiber laser based on transition metal dichalcogenides MoS_2, $MoSe_2$, WS_2, and WSe_2. Opt Express. 2015;23(20):26723–37.
[59] He GS, Xu GS, Prasad PN, Reinhardt BA, Bhatt JC, Dillard AG. Two-photon absorption and optical-limiting properties of novel organic compounds. Opt Lett. 1995;20(5):435–7.
[60] Luo ZC, Luo AP, Xu WC, Song CX, Gao YX, Chen WC. Sideband controllable soliton all-fiber ring laser passively mode-locked by nonlinear polarization rotation. Laser Phys Lett. 2009;6(8):582–5.
[61] Liu HH, Chow KK. Enhanced stability of dispersion-managed mode-locked fiber lasers with near-zero net cavity dispersion by high-contrast saturable absorbers. Opt Lett. 2013;39(1):150–3.
[62] Voropaev V, Donodin A, Voronets A, Vlasov D, Lazare V, Tarabrin M, et al. Generation of multi-solitons and noise-like pulses in a high-powered thulium-doped all-fiber ring oscillator. Sci Rep. 2019;9(1):18369.
[63] Fakhari M, Torkamany MJ, Mirnia SN. Linear and nonlinear optical properties of WO_3 nanoparticles synthesized at different fluences of pulsed Nd:YAG laser. EPJ Appl Phys. 2018;84(3):30401.
[64] Wang C, Wang L, Li X, Luo W, Feng T, Zhang Y, et al. Few-layer bismuthene for femtosecond soliton molecules generation in Er-doped fiber laser. Nanotechnology. 2018;30(2):025204.
[65] Li X, Xu W, Wang Y, Zhang X, Hui Z, Zhang H, et al. Optical-intensity modulators with PbTe thermoelectric nanopowders for ultrafast photonics. Appl Mater Today. 2022;28:101546.
[66] Ma W, Yin P, Li M, Sui L, Wang T, Liu Z, et al. Graphdiyne-decorated microfiber based soliton and noise-like pulse generation. Nanophotonics. 2021;10(16):3967–77.
[67] Pang L, Sun Z, Zhao Q, Wang R, Yuan L, Wu R, et al. Ultrafast photonics of ternary $Re_xNb_{(1-x)}S_2$ in fiber lasers. ACS Appl Mater Interfaces. 2021;13(24):28721–28.
[68] Li L, Pang L, Wang Y, Liu W. $W_xNb_{(1-x)}Se_2$ nanosheets for ultrafast photonics. Nanoscale. 2021;13(4):2511–8.
[69] Lin S-S, Hwang S-K, Liu J-M. High-power noise-like pulse generation using a 156-μm all-fiber laser system. Opt Express. 2015;23(14):18256–68.
[70] Xia H, Li H, Deng G, Li J, Zhang S, Liu Y. Compact noise-like pulse fiber laser and its application for supercontinuum generation in highly nonlinear fiber. Appl Opt. 2015;54(32):9379–84.
[71] Muller O, Gibot P. Optical limiting properties of templated Cr_2O_3 and WO_3 nanoparticles. Opt Mater. 2019;95:109220.